# NUMERICAL ASSESSMENT OF THE IMPACT AREA AND THE GEOMETRY OF A LANDSLIDE DAM: THE NAN-SHI-KENG LANDSLIDE, TAIWAN

Jian-Hong Wu [1*] and Ping-Hsuan Hsieh [2]

## ABSTRACT

This study predicts the impact area and the stability of a landslide dam of the moving Nan-Shi-Keng landslide in Taiwan for different joint friction angles using a three-dimensional distinct element code, 3DEC. When the landslide occurs, the sliding mass moves longitudinally along the basal sliding surface. Then, rocks spread laterally and ascend after they collide with the hill on the opposite side of the river. Increasing the joint friction angle substantially decreases the impact area and the height of the landslide dam. The computational results reduce the variation of the three-dimensional geometry of the landslide dam from that obtained using empirical formulas and suggest that the landslide dam is stable. The 3DEC is a potentially important tool for local disaster mitigation policy assessments of the impact of large landslides.

*Key words:* Anti-dip slope landslide, discrete element method, numerical simulation, distinct element method, landslide dam.

## 1. INTRODUCTION

The anti-dip slope is classified as the rock formation dipping approximately opposing to dip direction of the slope. Landslides occurring on anti-dip slopes have been reported in many different places in the world, such as Sahara in North Africa (Busche 2001), Putanpunas stream in Taiwan (Lo 2017), the Tangjiawan landslide in China (Fan *et al.* 2018), and the Nattai North landslide in Australia (Do and Wu 2020a). In the literature, most studies on the anti-dip landslide were focused on the local lithology and minerals (Busche 2001), triggering mechanism (such as intensive earthquake, river erosion, or mining activities) (Fan *et al.* 2018; Do and Wu 2020a), and slope stability (Fan *et al.* 2018; Yang *et al.* 2018).

Prediction of the impact area of an unstable landslide site is crucial to establish appropriate soft countermeasures. The prediction methods can be generally classified into empirical and numerical approaches. Although empirical prediction provides a quick evaluation of the impact area, it does not fully consider the local topography, which strongly affects the failure behavior and the depositional pattern of a landslide. Scheidegger (1973) proposed the relationship given in Eq. (1) to predict the run-out distance of a landslide on the basis of the landslide volume, but this neglected the impact of local topography.

$$\log \frac{h}{L} = -0.15666 \log V + 0.62419 \tag{1}$$

where $V$ is the volume of a possible landslide, and $L$ and $h$ are the horizontal distance and vertical distance between the two end points of the landslide, *i.e.,* from the crown to the farthest distance rock travelling. For predicting the length of a landslide dam, Nicoletti and Sorriso-Valvo (1991) classified catastrophic landslides into low-energy, moderate-energy, and high-energy dissipative landslides based on the total mechanical energy dissipation caused by the local morphology. The accuracy of the empirical formulas is highly dependent on historical data.

In numerical approaches, the local landform can be explicitly considered in the post-failure simulation of a landslide. Sliding rocks are simulated by a block assembly (such as in the discrete element method) or a viscous fluid (such as in the continuum approach). In the discrete element method (DEM), the sliding rocks are modeled as an assembly of spheres (Cundall and Strack 1979) or polyhedrons (Itasca 2016a; Wu *et al.* 2018; Wu and Hsieh 2021) with contact interactions. When the sliding rocks are simulated as an assembly of spheres, the complex judgment of contact between polyhedrons is simplified to be spheres, increasing the computational speed. However, the block geometry and surface friction angle are not consistent with the geometry of and the surface friction angle between blocks with planar boundaries in a real rock mass (Wu *et al.* 2018). In addition, the packing pattern affects the behavior of sphere assembly, which may not represent the real behavior of the in situ rock mass. In the polyhedron-based DEM, the geometry of the joints in the numerical simulation is explicitly presented and must follow the in situ rock mass. Complex judgment of contact between polyhedrons for simulating the post-failure behavior of a block assembly is time expansive, especially when the simulation includes more than ten thousand blocks travelling a long distance. In the continuum approach (Kuo *et al.* 2013), a rheology model dominates the post-failure behavior of a landslide, but appropriate parameters are hard to predict for a forward analysis of landslide simulation. In addition, a rheology model cannot easily describe the anisotropic behavior of joints in the rock mass.

Historical records indicate the ease with which failure of a

landslide dam occurs (Ermini and Casagli 2003) and that the geometry of a landslide dam is essential for assessing dam stability. Because the local landform and the mechanical properties of the rock mass strongly govern the geometry of the landslide dam, there is considerable variation in the estimation of the impact area of the landslide dam by empirical approaches (Ermini and Casagli 2003; Kuo *et al.* 2011). In this study, the impact area and the geometry of the landslide dam of the Nan-Shi-Keng landslide are assessed using the DEM, for the following reasons:

1. This landslide is moving continuously.
2. The landslide impact area and the geometry of the landslide dam have not been evaluated in the local disaster mitigation policy.

## 2. SITE DESCRIPTION

The Nan-Shi-Keng landslide is located adjacent to Tainan City Highway No. 175 (R-175) 25K+500 (23.205741°N, 120.46131°E) in Taiwan (Fig. 1). The R-175 is a priority emergency route that connects the Tseng-Wen Reservoir and the Wushantou Reservoir (Fig. 1(a)), and it is a main route linking residents living on the hillside area around the Tainan City center. The average slope angle in the study area is 20° in the northwest direction.

### 2.1 Local Geology

Geologically, the Nan-Shi-Keng slope is located between the Jhongkeng Fault and the Wushantou Fault (Fig. 1(a)). The rock strata at the landslide site belong to the Liuchungchi Formation, which is Pliocene–Pleistocene in age and made up mainly of mudstone and sandstone. The strike of the rock strata is approximately N15°E and their dip angle is 36-40°E. Fig. 1(b) shows the rock outcrop (at point P in Fig. 1(a)) on a slope in the north of the landslide site. Therefore, the landslide is located on an anti-dip slope. The red dashed line (Fig. 2(a)) indicates the extent of the sliding area based on published in situ investigations (Land Engineering Consultants Co. 2019), and the rock mass on the slope can be divided into three layers based on rock cores from five boreholes (boreholes 17-4, 17-5, 17-6, and BH-1, BH-3) drilled on the lower slope of the highway (Fig. 2(b)) (Chen 2018; Cheien 2019; Land Engineering Consultants Co. 2019). The rock mass of the sliding area shown along the profile of A-A′ in Fig. 2(a) is as follows (Fig. 2(b)):

1. Top layer: thin matrix-controlled yellowish colluvium at shallow depths with occasional large sandstone blocks (for which the standard penetration test blow count (SPT-N) is 5 − 20);
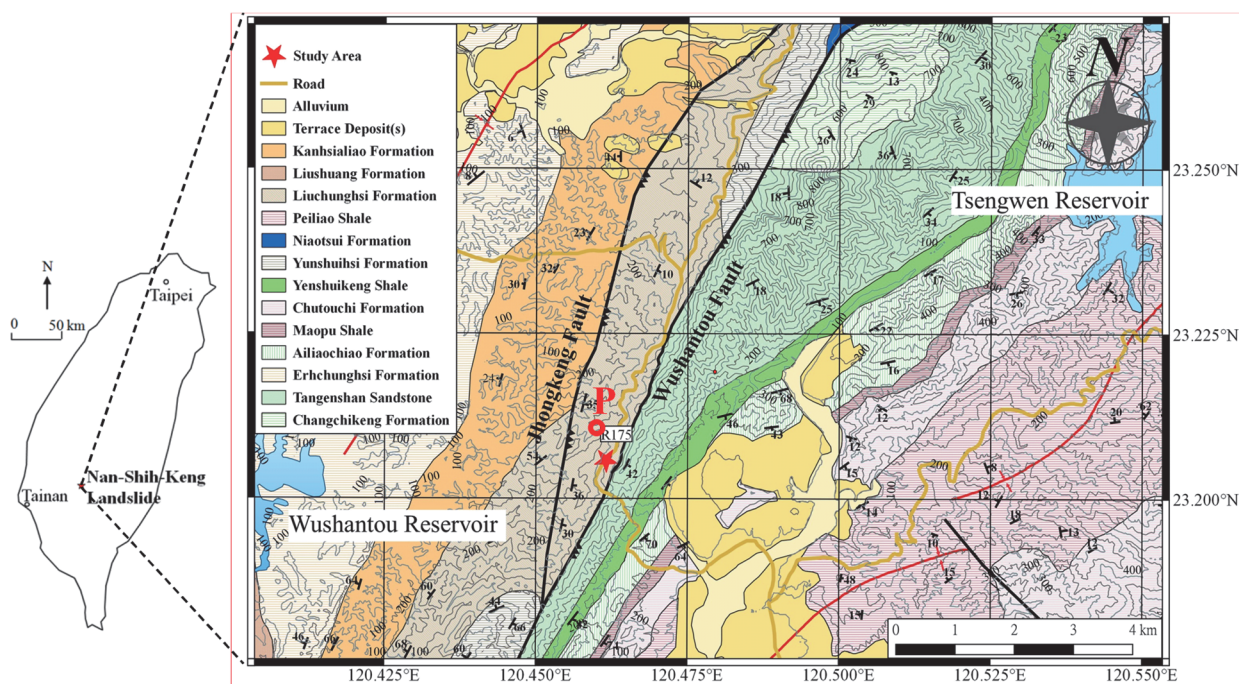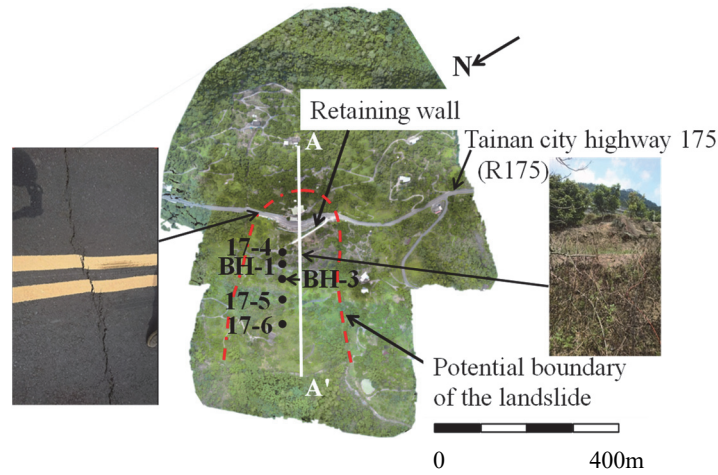


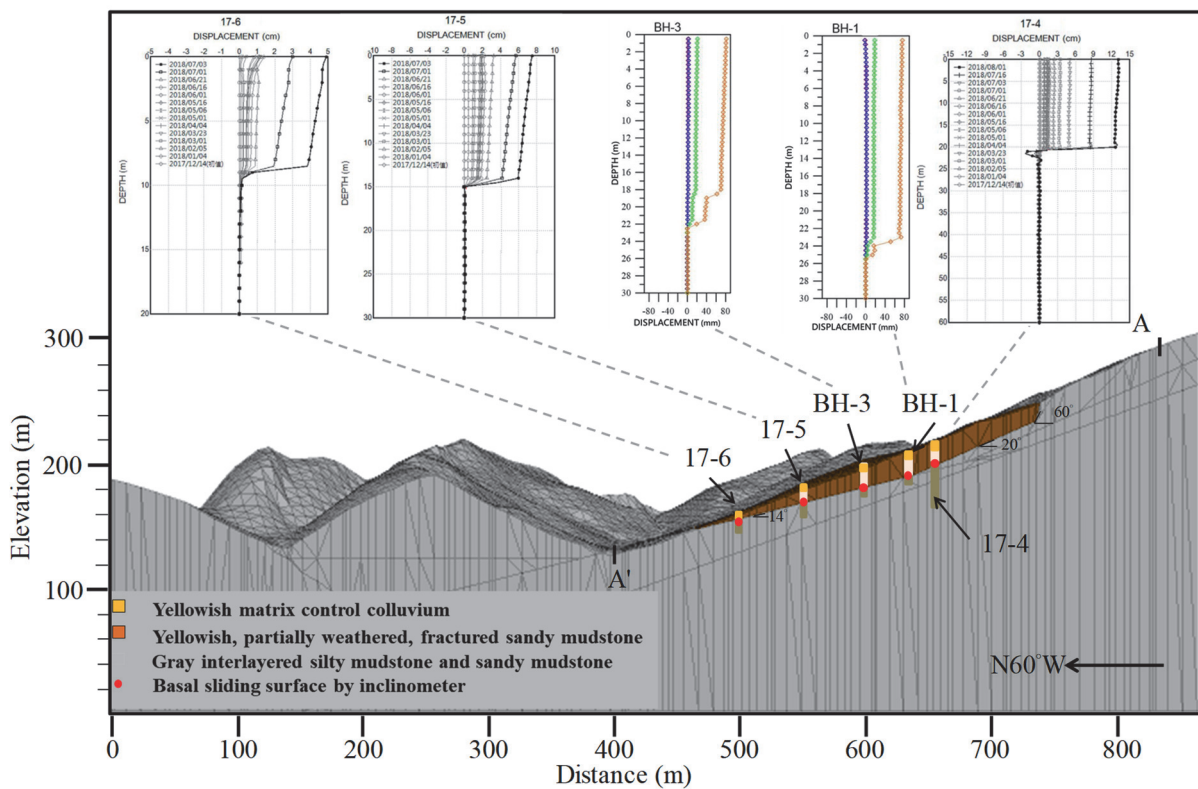(a) Geological map of the study area



(b) Picture showing the eastward dipping rock layer at the north of the landslide (Point P in Fig. 1(a))

**Fig. 1　Local geology and anti-dip slope picture at the Nan-Shi-Keng landslide**

(a) Bird view of the slope and the locations of the inclinometer boreholes



(b) Geometrical profile along A-A′ with sliding rocks and fixed rock mass

**Fig. 2   Locations of the inclinometers on the Nan-Shi-Keng landslide**

2.  Middle layer: yellowish, partially weathered, fractured sandy mudstone (for which SPT-N is usually $11 - 20$ but occasionally larger than 100, and for which the rock quality designation (RQD) is $30 - 70$);

3.  Bottom layer: gray interlayered silty mudstone and sandy mudstone (for which SPT-N is above 100 and RQD is $60 - 100$). The dip angle of the bedding of the core is $35° - 65°$ (Land Engineering Consultants Co. 2019), which is consistent with measurements on rocks at the surface.

Based on inclinometer monitoring data (Chen 2018; Land Engineering Consultants Co. 2019) (Fig. 2(b)), the basal sliding surface is located within the upper section of the bottom layer or at the boundary between the middle and bottom layers.

## 2.2   Previous Slope Failures

Since the highway started to be operated in 1980, the slope between the mileage of 25K + 450 and 25K + 550 has been unstable. Su (2007) and Chang (2013) concluded the disaster history of the slope. In 1986, the slope started to deform significantly. The roadbed sunk during every typhoon or heavy rainfall. In 1991, the road sunk seriously due to a heavy rainfall. The highway maintenance authority shifted the route close to the mountain side. However, the typhoons and heavy rainfall continuously impacted the highway stability by triggering the settlement and cracks on the pavement during the rainy season from May to November. In July 1998, the heavy rainfall sunk the roadbed and retaining wall by 1.5 m. The local traffic was blocked. Comprehensive in-situ investigations,

borehole drillings, and monitoring started to clarify the mechanism and mitigate the slope deformation. Engineers designed a larger slope stability protection hard measure, which was completed in 2000. The roadbed and the highway slope survived during the heavy rainfalls induced by the typhoon of Toraji (2001) and Nari (2001). Unfortunately, the road was damaged again by typhoon-induced heavy rainfalls since August 2003. New investigations, rectification designs and monitoring started. The first phase of monitoring work was carried out from October 2005 to May 2006. The emergency reinforcement and improvement project of the instable slope was completed in February 2007. The second phase of monitoring work was finished in 2009. The road slid during Typhoon Kalmaegi (2008), Typhoon Morakot (2009) and other heavy rainfalls. The highway maintenance authority added piles and pre-stressed anchors to increase the stability of retaining wall in mid-February 2012. However, cracks on the highway (Fig. 2(a)) and exposing of the upper part of piles showed the significant slope movement in 2018. In addition, the narrow creek channel near the toe of the landslide (Fig. 2(b)) shows the possibility to generate a landslide dam after the landslide occurs.

Observations made in June, 2018 of cracks on the highway pavement (Fig. 2(a)), where it borders the landslide, and in-situ monitoring results of a long-range wire extensometer (Chien 2019) and an inclinometer on the lower part of the slope (Chen 2018; Chien 2019; Land Engineering Consultants Co. 2019) indicate that the slope moves continuously and parallel to the dip direction toward 300° of the slope. So far, engineers have succeeded in protecting the R-175 as well as farmhouses and orchards situated on the upper and lower slopes of the highway through the use of retaining walls and drainage systems. However, the post-failure behavior of the landslide has not been studied even though the landslide may generate a landslide dam, which could greatly impact the safety of downstream villages and the water source of the Wushantou reservoir.

## 3. NUMERICAL AND EMPIRICAL APPROACHES TO LANDSLIDE DEPOSITION

The objective of this study is to predict the possible impact area of the Nan-Shi-Keng landslide based on detailed in situ observations (Kao 2006; Land Engineering Consultants Co. 2006; Su 2007; Chang 2013; Chung *et al.* 2013; Kao *et al.* 2014; Chien 2019) and numerical simulations. The accuracy of the impact area prediction using numerical simulations is validated by empirical approaches. The height and width of the landslide dam calculated by the numerical simulations are then compared with those obtained from statistical data and empirical formulas to assess the stability of the landslide dam.

### 3.1 Numerical Approach

Discrete element methods (Wu 2010; Wu *et al.* 2017a, 2017b, 2018; Chen and Wu 2018; Do and Wu 2019; Do and Wu 2020b, 2020c; Wu and Hsieh 2021) are numerical approaches that can successfully simulate the post-failure behavior of different rock avalanches. The distinct element method, which is a member of the DEM family, models component rocks using polyhedrons.

The 3DEC (version 5.2) modeling software is a three-dimensional (3D) numerical program using the distinct element method to simulate the contact between polyhedrons with planar boundaries. In the Nan-Shi-Keng landslide, the 3D landform geometry of the valley controls the movement and the deposition of the sliding blocks. Therefore, the impact area of the landslide is evaluated using 3DEC.

In the DEM, the behavior of both blocks and contacts at discontinuities must be considered. In this study, the blocks are assumed to be rigid because movement along discontinuities between blocks accounts for most of the deformation in the rock mass.

In 3DEC, the unknowns of each block (denoted by block *i*) are the translational displacement and the angular displacement at the block centroid in 3D coordinate directions (Hart *et al.* 1988). Equations (2a) and (2b) are the governing equations for each block in each time step.

$$\bar{a} = (\sum \bar{F}) / m \tag{2a}$$

$$\bar{\alpha}_a = (\sum \bar{M}) / \bar{I} \tag{2b}$$

where *m* is the block mass, $\bar{a}$ is the acceleration vector, $\bar{F}$ indicates the summation of external forces, $\bar{\alpha}_a$ is the angular acceleration vector, $\bar{M}$ represents the summation of moments, and $\bar{I}$ indicates the moment of inertia of each block.

Figure 3 shows the calculation cycle in 3DEC. The force-displacement law indicates that forces arise due to the block displacements. The force-displacement laws are taken as incremental: that is, a change in displacement produces a change in force that is added to the existing force stored for that contact. In one time step, the incremental shear and normal displacements for a given contact are evaluated from the incremental 3D displacements at each block. New shear and normal forces are then calculated from the previous forces using incremental forces calculated from the force-displacement equations. These contact forces are then resolved into equivalent 3D forces and moments and added to the other 3D forces and moments acting on each block. The equation of motion in Fig. 3, that is, the summation of the force built up at each block, is used to compute block accelerations, $\bar{a}$, in 3D by Eq. (2). The accelerations are numerically integrated to obtain velocities, which are further integrated to give displacements. With this new set of displacements, the calculation proceeds with the next time step.

In 3DEC, the common plane (*c-p*) is used to determine the contacts between blocks (Cundall 1988). Figure 4 shows the position of the *c-p* in response to the block geometry. The *c-p* is located midway between the centroids of the two blocks, with a unit normal vector pointing from one centroid to the other. When block contact occurs in 3DEC, the normal contact spring, $k_n$, and normal contact damper, $\eta_n$, are connected in parallel (Fig. 5(a)). In addition, in the shear direction, the shear contact spring, $k_s$, and shear
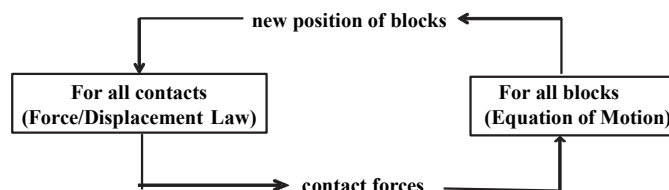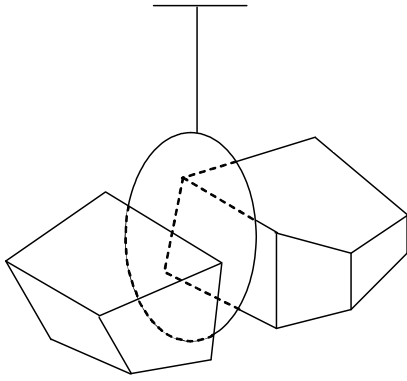


**Fig. 3   Calculation cycle of DEM (Cundall 1988)**

**Fig. 4    Sketch of common-plane in 3D DEM (Cundall 1988)**

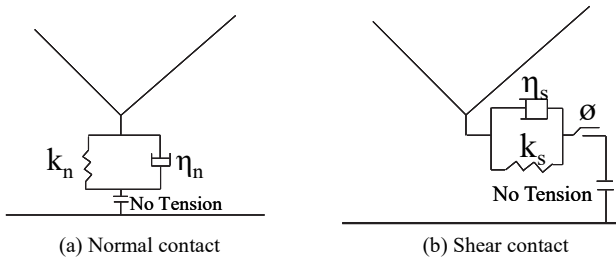

(a) Normal contact         (b) Shear contact

**Fig. 5    Mechanical behavior of contacts in DEM**

contact damper, $\eta_S$, are connected in parallel and connected to the Coulomb slider, $\phi$ (Fig. 5(b)). Both contact springs and contact dampers are numerical parameters. The details of 3DEC theory and calculation algorithms are described in Cundall (1988), Hart *et al.* (1988), and Itasca (2016a).

## 3.2    Empirical Approach

The Nan-Shi-Keng landslide is geomorphologically classified as a high-energy dissipative landform (Fig. 1) because of the narrow river channel at the slope toe and a hill at the opposite side of the slope (Nicoletti and Sorriso-Valvo 1991). The width of the landslide dam can be calculated from:

$$W/W_a = 0.21 - 0.51 \tag{3}$$

where $W$ is the landslide width and $W_a$ is the landslide dam width. Tsai *et al.* (2016) gave an alternative estimate for the landslide dam width in Taiwan using:

$$W_a/W = 1.5 - 2.0 \tag{4}$$

In addition, Kuo *et al.* (2011) and Van Woerden (2018) investigated landslide dams triggered by heavy rainfalls in Taiwan and New Zealand, respectively, and their correlations between the volume and height of a landslide dam are plotted in Fig. 6. The landslide dam in New Zealand is higher than the Taiwan dam even though the dam volumes are the same. The empirical assessment of the landslide dam height is site dependent, which means that it is controlled by the mechanical properties of the local rock mass and geometry of local topography. In addition, it is practically difficult to use Fig. 6 to predict the dam height from the volume of the dam because, as shown by Ermini and Casagli (2003), there is a wide variation in the proportion of landslide volume involved in dam formation, ranging from approximately 100% to less than 1%. Therefore, in the empirical approach, the landslide volume can only be assumed to be the maximum volume of a landslide dam when predicting the maximum height of the landslide dam.
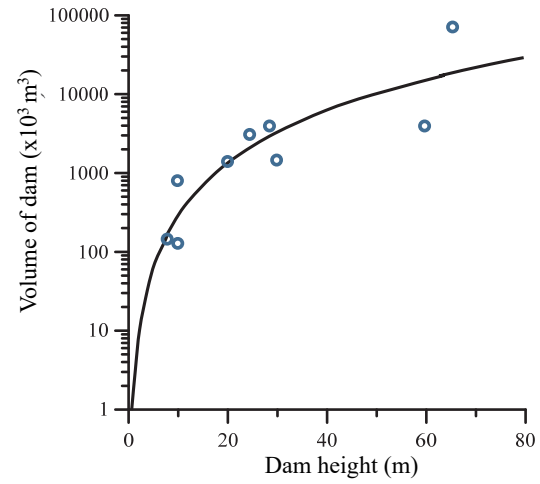


(a) Dam in Taiwan (modified from Kuo *et al.* 2011)
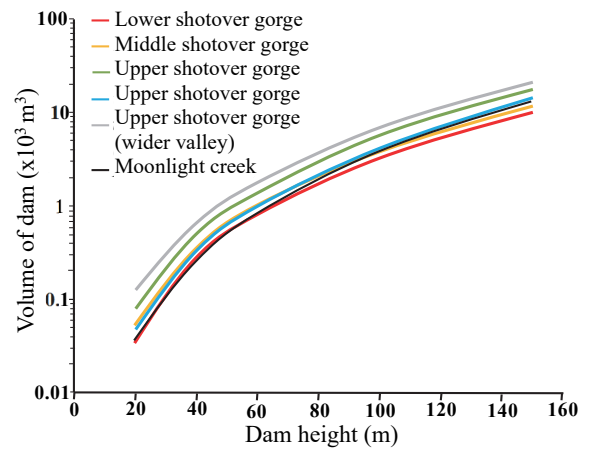


(b) Dam in New Zealand (van Woerden 2018)

**Fig. 6    Statistical relation between volume of dam and dam height**

## 4.    NUMERICAL SIMULATION

### 4.1    Geometrical Considerations

Triangular prisms were applied to generate the 3D terrain in 3DEC. The top and the side views of the local 3D topography and the source area of the landslide are shown in Figs. 7(a) and 7(b), respectively. The triangles in Fig. 7 indicate the three monitoring points (the crown and road are at the ground surface, while the lower slope is located at the middle elevation of the sliding rocks), and the red dots represent local farm houses. Figure 2(b) shows the geometric cross section along the dip direction of the slope toward 300° in 3DEC. The gray blocks represent the fixed slope rock mass and the brown blocks represent the inferred sliding rocks and soil. Unstable geomorphic precursors and disaster histories define landslide boundaries on the ground surface (Kao 2014). A 300-m electrical resistivity survey of the transverse section of the landslide near the toe of the highway retaining wall conducted using the pole-pole method with an electrode interval of 5 m showed a trapezoidal cross section of the sliding rocks and soil (Land Engineering Consultants Co. 2006) and a 30° dip angle of the two legs. The basal sliding surface along the A-A′ cross section in Fig. 2(a) is divided into three sections to simulate the curved basal sliding surface (Fig. 2(b)):

1. Section 1: The sliding surface at the crown dips at 60° toward 300°.

2. Section 2: The siding surface in the middle dips at 20° toward 300°. The surface was obtained by connecting sliding surfaces measured in boreholes BH-1 and 17-4;

3. Section 3: The sliding surface along the downslope dips at 14° toward 300°. The surface corresponds to the sliding surface from inclinometer data from boreholes 17-6, 17-5, BH-3, and BH-1;

In Fig. 2(b), the sliding rocks comprise colluvium, fractured rocks, and part of the inherent silty or sandy mudstones. While the matrix-controlled colluvium governs the top layer of the rock mass, the joints and beddings in the middle and bottom rock layers dominate the sliding rocks and soil. The colluvium at shallow depths in the landslide site makes it difficult to clarify the discontinuity geometries in the sliding rock mass. In addition, clear orientation of the discontinuities in the cores has not been reported (Chang 2013). Chigira (2013) proposed that two joint sets that strike parallel and in the longitudinal direction of the landslide slope are usually observed in deforming landslides. Therefore, in this study, the following discontinuity sets cut the sliding rock mass as shown in Fig. 8(a). The geometrical relation between the discontinuity sets and slope is shown by the stereo net in Fig. 8(b) and is summarized below.

1. Joint Set 1 (Js1): The joint set is at 90° toward 38°; it trends northwest-southeast parallel to the landslide boundaries on the ground surface and corresponds to the discontinuities striking in the longitudinal direction of the slope.
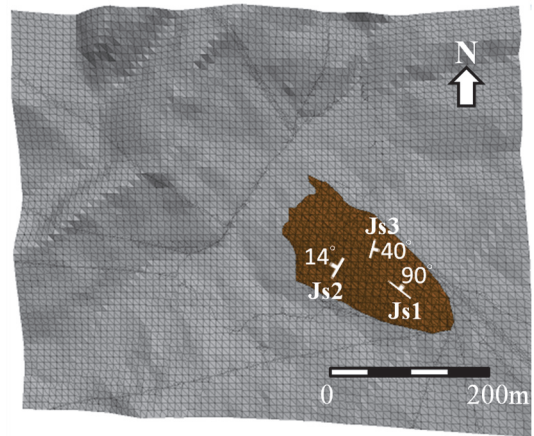


(a) Three joint sets in the sliding rock mass
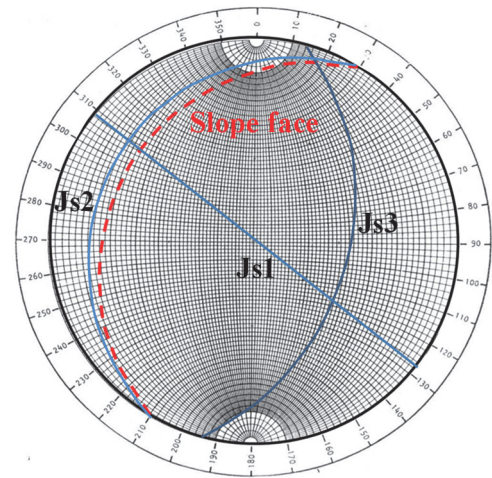


(b) Stereo-net of the joint sets and slope

**Fig. 8   Geometries of joint sets and sliding plane**

2. Joint Set 2 (Js2): The joint set is at 14° toward 300° and is parallel to section 3 of the basal sliding surface. Js2 corresponds to the discontinuities striking parallel to slope.

3. Joint Set 3 (Js3): The joint set is at 40° toward 105°, which corresponds to the bedding of the local anti-dip slope formation.

The landslide width, which is the maximum width of the sliding zone, is 116 m, as measured from the sliding zone of the numerical model. The spacing of each joint set (Jsp) in this study was assumed to be 5 m to complete computations within a reasonable time. In the 3DEC simulations, the volume of the sliding rocks is 279,758 $m^3$, and the total number of sliding blocks is 9696.

### 4.2   Parameter Installations

Parameters for the 3DEC simulations include physical and mechanical parameters and numerical parameters. Table 1 lists the parameters used in this study. Physical and mechanical parameters relate to the properties of blocks and discontinuities, whereas numerical parameters are applied to ensure numerical stability in the 3DEC simulations.

#### 4.2.1   Physical and Mechanical Parameters

Figure 1(a) shows that the sliding slope, the valley near the slope toe, and the opposite slope constitute the Liuchungchi
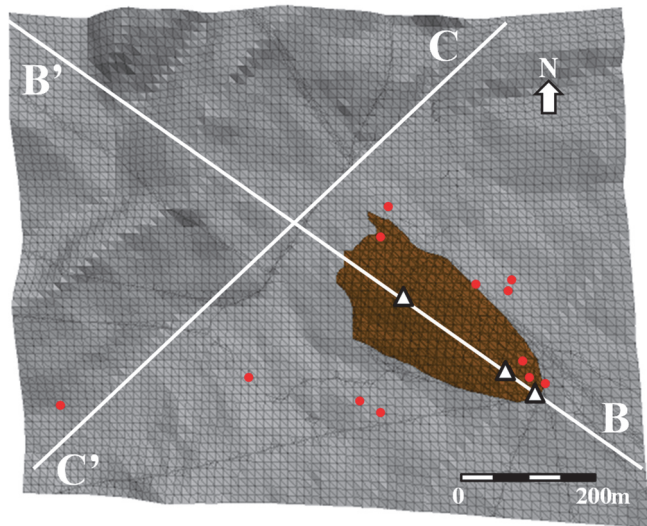


(a) Top view (red dots are the farmhouses)
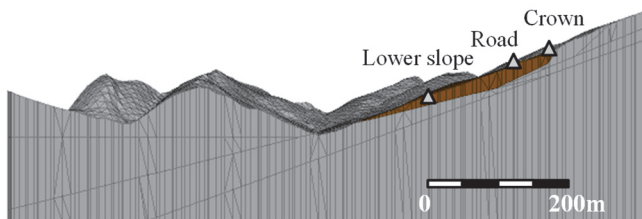


(b) Side view (triangles are the monitoring points)

**Fig. 7   Geometry of the local topography and the sliding blocks**

Formation. One set of physical properties applies to all blocks, and one set of joint mechanical properties applies to all joints and ground surfaces (Table 1). The block density is set at 2,200 kg/m³ (Kao 2006), and the driving gravity is 9.8 m/s². The normal direction and shear direction of joints follow the elastic spring model and Coulomb-slip joint model, respectively, in the total stress (Itasca 2016a). The slope is moving, and the joints are assumed to be in the residual state and the joint cohesion is 0 kPa. Table 2 shows the range of friction angle of the soil in the colluvium ($\phi = 15.0° - 23.3°$) and the weak planes of rocks ($\phi = 21.0° - 33.6°$), which were obtained from the literature. The mean of the friction angles of the soil of the colluvium and the weak plane of rocks are 19.6° and 22.1°, respectively. Therefore, the mean value of the friction angle of the weak plane of rocks is 2.5° higher and has a wider variation than that of soil in the colluvium. In this study, the friction angles of the colluvium zone and the fractured rock zone are assumed to be the same to simplify the calculation. The joint friction angle is assumed to be less than 14°, which is the dip angle of the basal sliding surface of Js2 described in Section 4.1 because the post-failure simulation is the main target of this study. Pore pressure fluctuations associated with the joint movement are not explicitly considered. By sensitivity analysis, the effect of pore pressure is simulated by decreasing joint friction angles. Therefore, the simulation with the worst scenario, $\phi = 10°$, was conducted first. Subsequently, sensitivity analysis was performed to investigate the effect of three cases of friction angles of all the joints and surfaces on the impact area and the geometry of the landslide dam:

1. Case 1: $\phi = 10°$; this is the minimum value from the direct shear tests on a joint adjacent to the basal sliding surface (Kao 2006), and it corresponds to the worst scenario of the post-failure simulation.

2. Case 2: $\phi = 12°$.

3. Case 3: $\phi = 14°$; this is the smallest dip angle of the moving basal sliding surface (Fig. 2(b)) and can be considered the upper bound of the joint friction angle to the post-failure simulation.

**Table 1    Parameters for the numerical analysis**

| Item | | Value | Remarks |
|---|---|---|---|
| Physical and mechanical parameters | | | |
| Block | Density (kg/m³) | 2,200 | Kao 2006 |
| Joint | Cohesion (kPa) | 0.0 | |
| | Friction angle (°) | 10, 12, 14 | Table 2 |
| | Tensile strength (kPa) | 0.0 | |
| Numerical parameters | | | |
| Normal contact spring stiffness, $k_n$ (Pa/m) | $3 \times 10^7$ | Shear contact spring stiffness, $k_s$ (Pa/m) | $3 \times 10^7$ |
| Normal contact damper, $\eta_n$ (MNsec/m) | 0.0 | Shear contact damper, $\eta_s$ (MNsec/m) | 0.0 |

**Table 2    Friction angle of the joints and soils of the study site**

| Sample | Friction angle (°) | Test method | Reference |
|---|---|---|---|
| Soils in the colluvium | 15.0 – 19.5 | Triaxial tests | Chang (2013) |
| | 23.3 | Back calculation from numerical simulations | Chung *et al.* (2013) |
| Rocks containing weak plane | 21.0 – 33.6 | Direct shear tests | Chang (2013) |

### 4.2.2   Numerical Parameters

In 3DEC, to increase the numerical stability in the dynamic calculations, numerical parameters including time step, damping constant, and contact spring stiffness are considered. The time step is calculated automatically by the 3DEC. Determining the appropriate damping constants has the following two difficulties:

1. When they are physical parameters, suitable damping constants cannot be obtained for the computations without conducting in situ tests. Unfortunately, we did not conduct in situ tests or obtain in situ damping data;

2. When they are numerical parameters, to mitigate unwanted vibrations in the discrete element calculations, block contacts change remarkably in each step with large block displacement.
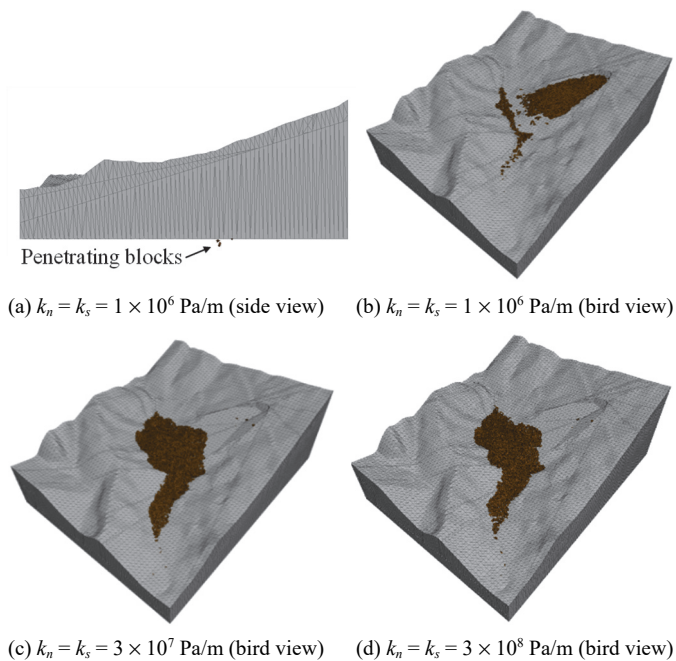
In addition, the time increment in each time step significantly governs the system vibration. Therefore, the numerical vibration pattern changes remarkably in each step, and it is difficult to predict the suitable damping constants to properly mitigate the unwanted system vibration in each step. In this study, numerical damping is not considered in the simulations in order to reduce the number of numerical parameters.

The solution for the distinct element method is only conditionally and numerically stable if the time increment $\Delta t$ is less than the critical value, $\Delta t_{critical}$. The critical time increment can be determined by the inter-block relative displacement, which can be determined by calculating the limiting time increment from the mass of the smallest block in the system, $M_{min}$, and the maximum contact stiffness, $K_{max}$, in Eq. (4) (Itasca 2016a):

$$\Delta t_{\text{critical}} = FRAC \times 2 \left( \frac{M_{\min}}{K_{\max}} \right)^{1/2} \tag{4}$$

where *FRAC* is a user-defined factor that accounts for the fact that a block may be in contact with several blocks with a default value of 0.1 (Itasca 2016a).

In this study, contact spring stiffness is a numerical parameter to ensure both numerical stability and large critical time increment to complete the post-failure simulation. Because the mass of the smallest block, $M_{min}$, in a blocky system is determined physically on the basis of block volume and density, a soft contact spring increases the critical time increment. Then, the post-failure behavior of a landslide can be simulated by fewer calculation steps. In addition, a soft contact spring also decreases the unwanted contact vibrations and the calculation cycles for a system to approach the equilibrium state (Cundall and Strack 1979). The contact spring stiffness $k_n = k_s$ ensures an elastic contact (Cundall and Strack 1979). However, if the contact spring stiffness is too small, insufficient contact force results in abnormal block penetration in the calculations. Therefore, the appropriate value of contact spring stiffness is determined by trial and error based on the following two criteria: no block penetration and no abnormal block movement, such as abnormal block flying, can occur in the landslide simulation. In Fig. 9(a), some sliding rocks penetrate to the bottom blocks when $k_n = k_s = 1 \times 10^6$ Pa/m and $t = 13$ s. In addition, when $t = 50$ s, the simulation result of final block deposition with $k_n = k_s = 1 \times 10^6$ Pa/m (Fig. 9(b)) is different from those with $k_n = k_s = 3 \times 10^7$ Pa/m (Fig. 9(c)) and $3 \times 10^8$ Pa/m (Fig. 9(d)). Although the simulation results with $k_n = k_s = 3 \times 10^7$ Pa/m (Fig. 9(c)) and

(a) $k_n = k_s = 1 \times 10^6$ Pa/m (side view)    (b) $k_n = k_s = 1 \times 10^6$ Pa/m (bird view)



(c) $k_n = k_s = 3 \times 10^7$ Pa/m (bird view)    (d) $k_n = k_s = 3 \times 10^8$ Pa/m (bird view)

**Fig. 9    Simulation results with different contact spring stiffness**

$3 \times 10^8$ Pa/m (Fig. 9(d)) are similar, in this study, the former condition is considered for the sequential 3DEC simulations because a soft contact spring results in high numerical stability and lower computational cost.

### 4.3    Boundary Condition

The gray blocks in Fig. 9 are fixed by setting the zero velocities at the centroid point of each block (Itasca 2016b). In addition, when blocks are in contact to each other, the joint boundaries of the sliding blocks and those between the sliding blocks and fixed blocks also follow the Coulomb-slip joint model and the elastic spring model in the directions parallel and normal to the joint, respectively (Itasca 2016a). The physical parameters of the joints are shown in Table 1.

## 5.    COMPUTATION RESULTS

### 5.1    Landslide Simulation with $\phi = 10°$

Figure 10 shows the landslide process with $\phi = 10°$ in the 3DEC simulations. At the beginning of the landslide ($t = 10$ s), the blocks slide mainly parallel to the dip direction of the basal sliding surface (Fig. 10); this sliding direction is very close to the dominant sliding direction given by the inclinometer data. At 15 s (Fig. 10(b)), the sliding blocks climb the opposite slope. At 20 s (Fig. 10(c)), the sliding blocks spread laterally upstream and downstream of the Nan-Shi-Keng creek. Lastly, at 50 s, the final deposition of the sliding blocks is as shown in Fig. 10(d). In this study, the simulation is terminated when the velocity of each block decreases below 1 m/s (Fig. 11(a)). Most sliding rocks move 100 m to 300 m by the end of the landslide (Fig. 11(b)). Figure 11(c) shows the time-dependent velocity changes of the three monitoring points (crown, road, and lower slope) with maximum values of 14.11 m/s, 19.74 m/s, and 18.11 m/s at 30.96 s, 24.78 s, and 14.11 s,



(a) time = 10s



(b) time = 15s



(c) time = 20s



(d) time = 50s
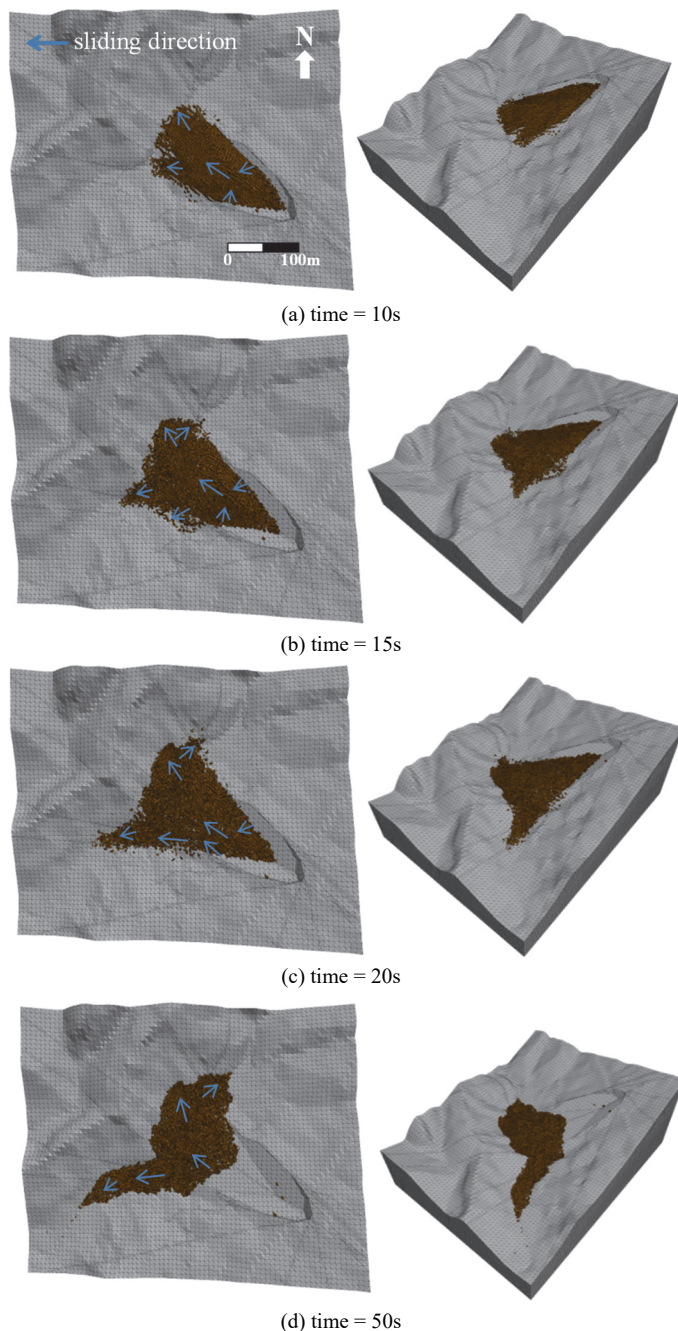
**Fig. 10    Failure process of the Nan-shi-keng landslide with $\phi = 10°$**
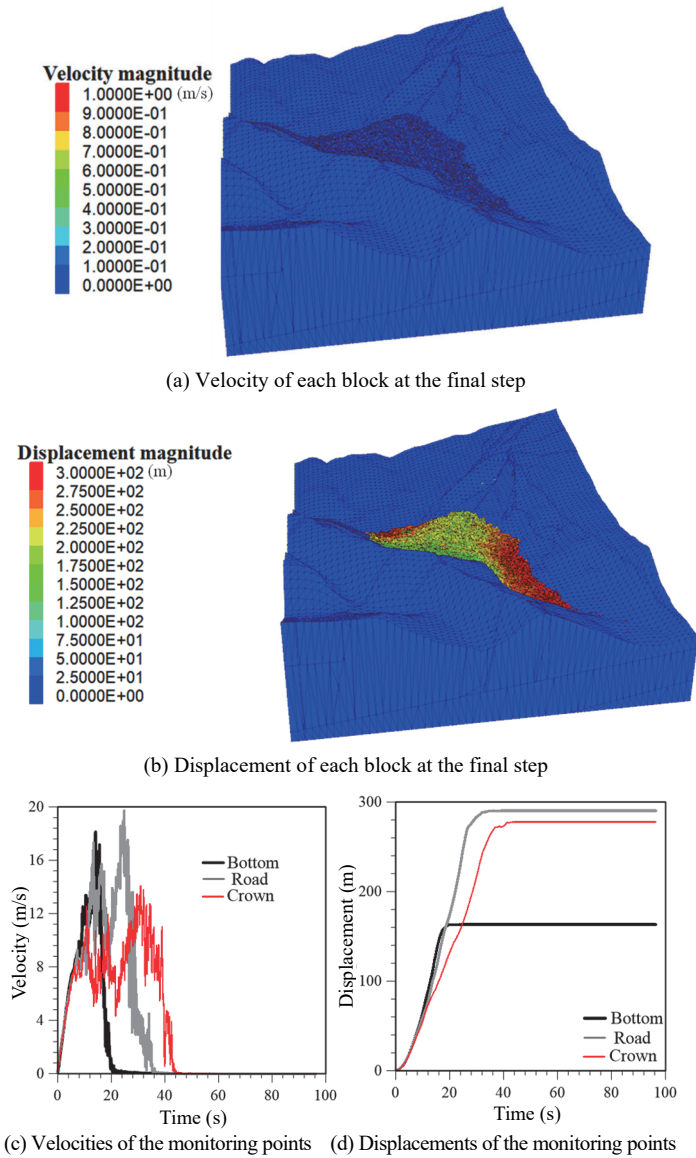
respectively. In addition, the final displacements of the three monitoring points are 277.51 m, 290.06 m, and 162.85 m, respectively (Fig. 11(d)).

### 5.2    Sensitivity Analysis of the Joint Friction

In this section, landslide simulations with $\phi$ equal to 12° and 14° are added to discuss the effect of the joint friction angle on the landslide behavior. Many sliding rocks remain on the slope at the end of the calculations when the angle is 12° and 14° (Fig. 12). Compared with the case where $\phi = 10°$ (Fig. 11(b)), the dominant block displacements depositing on the slope are $100 - 200$ m (in green) when $\phi = 12°$ (Fig. 12(a)) and $50 - 75$ m (in blue) when

(a) Velocity of each block at the final step



(b) Displacement of each block at the final step



(c) Velocities of the monitoring points    (d) Displacements of the monitoring points

**Fig. 11** **Computational block velocity and displacement with** $\phi = 10°$

of the deposit zone, and the horizontal distance that the rocks climb on the opposite slope increase as the joint friction angle decreases. The red hollow circles represent the farmhouses that may be impacted by a future Nan-Shih-Keng landslide. The red dots represent the houses with low possibility of being impacted by the landslide.
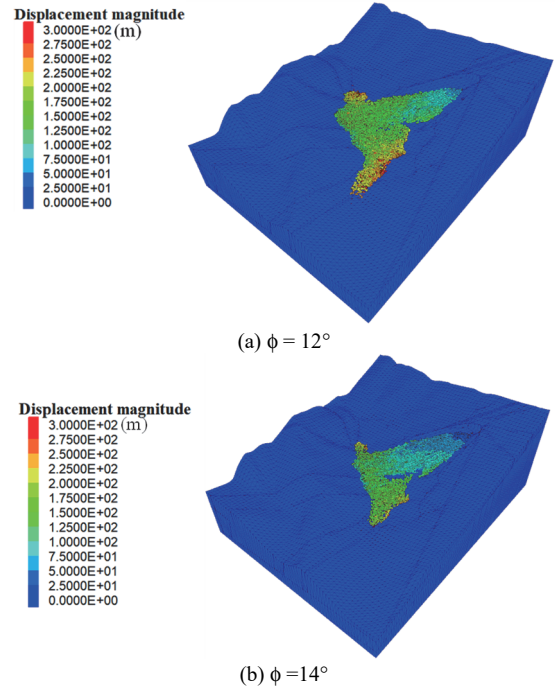


(a) $\phi = 12°$



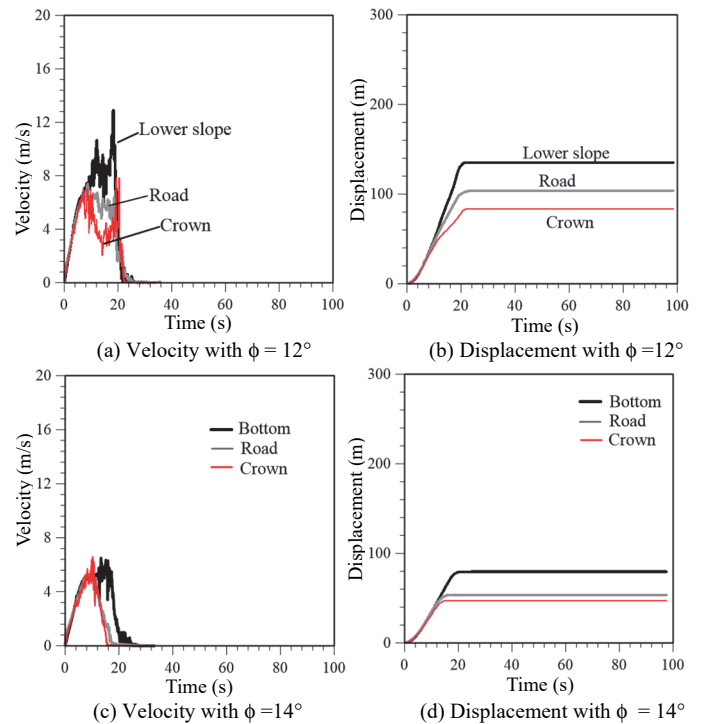(b) $\phi = 14°$

**Fig. 12** **Final displacement of each block**

$\phi = 14°$ (Fig. 12(b)). In addition, the number of blocks with displacement exceeding 250 m (in red) decreases as the joint friction angle increases.

When $\phi = 12°$, the maximum velocities of the three monitoring points (crown, road, and lower slope) are 7.85 m/s, 7.40 m/s, and 12.93 m/s at 19.33 s, 8.66 s, and 18.30 s, respectively (Fig. 13(a)). In Fig. 13(b), the final displacements of the three monitoring points are 83.52 m, 103.73 m, and 135.15 m, respectively. When $\phi = 14°$, Fig. 13(c) shows that the maximum velocities of the three monitoring points are 6.60 m/s, 5.28 m/s, and 6.52 m/s at 10.21 s, 9.07 s, and 13.28 s, respectively. The final displacements of the three monitoring points are 47.39 m, 53.50 m, and 79.31 m, respectively. Comparison of Figs. 11(c) and 11(d) with Fig. 13 indicates that the maximum velocities and displacements of each monitoring block decrease as the joint friction angle increases.
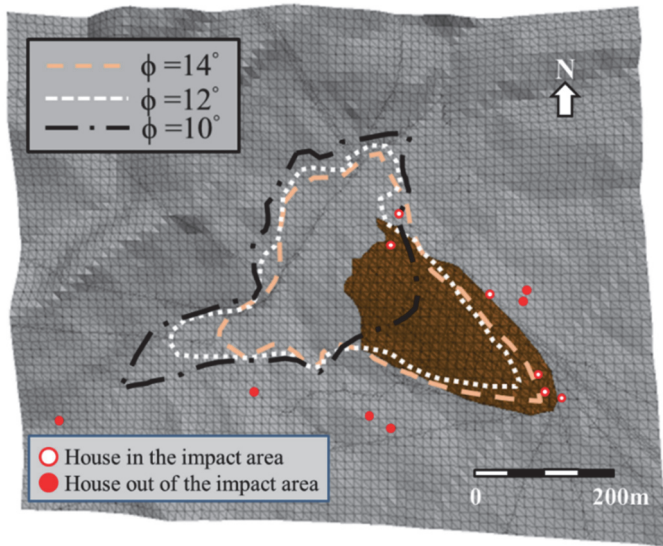
Figure 14 shows the impact area of the landslide at different joint friction angles ($\phi = 10°$, 12°, and 14°) simulated by 3DEC and the locations of possible damage to the local farmhouses. The rock volume sliding into the river channels, the lateral spreading



(a) Velocity with $\phi = 12°$    (b) Displacement with $\phi = 12°$



(c) Velocity with $\phi = 14°$    (d) Displacement with $\phi = 14°$

**Fig. 13** **Computational block velocity and displacement with** $\phi = 12°$ **and 14°**

**Fig. 14　The impact area of sliding blocks with different joint friction angles**

In addition, computation results confirm that the landslide generates a landslide dam (Figs. 14 and 15). The width of the landslide dam, $W_a$, is defined to be the longest distance of the highly concentrated deposited blocks in the simulation and is 478 m (for $\phi = 10°$; Fig. 15(a)), 355 m (for $\phi = 12°$; Fig. 15(b)), and 300 m (for $\phi = 14°$; Fig. 15(c)).

In the case of $\phi = 10°$, the side view along the profile B-B′ in Fig. 7(a) shows that the dam height (Fig. 16(a)) is 21 m in the valley, and the horizontal deposit distance is 191 m. When $\phi = 12°$ and 14°, the dam height along B-B′ (Fig. 7(a)) in the valley is 14 m (Fig. 16(b)) and 9.4 m (Fig. 16(c)), respectively. In addition, the horizontal deposit distance is 336 m (Fig. 16(b)) and 354 m (Fig. 16(c)), respectively.

The deposits thickness along profile C-C′ (Fig. 7(a)) in Fig. 17 can be divided into two groups according to the thickness. When $\phi = 10°$ (Fig. 17(a)), the deposit thickness is 20 m in the upstream and 7 m in the downstream areas. When $\phi$ increases to 12° and 14°, the deposit thickness in the upstream region changes to 15 m (Fig. 17(b)) and 12 m (Fig. 17(c)) and that in the downstream region decreases to 5 m (Fig. 17(b)) and 0 m (Fig. 17(c)).

Using empirical approaches, the landslide dam width, $W_a$, was estimated to be $232 - 552$ m from Eq. (3) (Nicoletti and Sorriso-Valvo 1991) and $174 - 232$ m from Eq. (4) (Tsai *et al.* 2016). In Figs. 15(a) to 15(c), the minimum and the maximum landslide dam widths from the empirical formulas are shown as a red line and the summation of the red and yellow lines, respectively. All scenarios ($\phi = 10°$, 12°, and 14°) show that the landslide dam width yielded by the 3DEC analysis is close to the results obtained from the empirical formula of Nicoletti and Sorriso-Valvo (1991) but substantially larger than the results obtained from the empirical formula of Tsai *et al.* (2016).

In addition, the height of the landslide dams in Taiwan is statistically calculated as $0 - 10$ m (Fig. 6(a)). Clearly, assessing the height of the landslide dam following Kuo *et al.* (2011) is difficult, especially for the prediction of a landslide, because the dam volume is unknown. In this study, the landslide volume is assumed to be the maximum dam volume in Kuo *et al.* (2011). Regarding the 3D depositional geometry after the landslide obtained from the
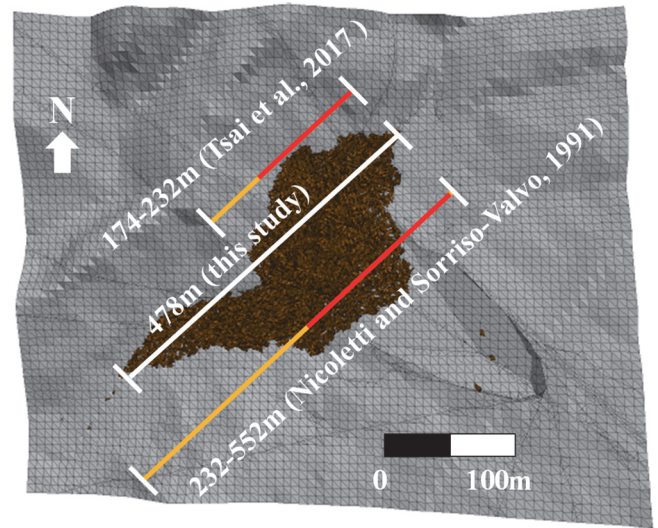


(a) $\phi = 10°$
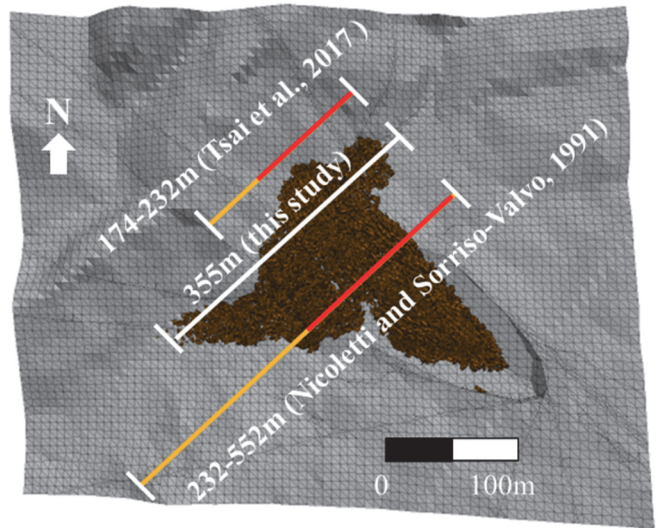


(b) $\phi = 12°$
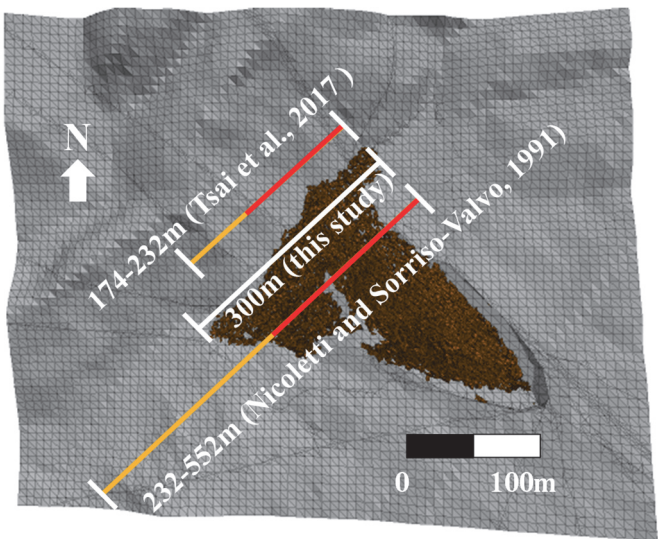


(c) $\phi = 14°$

**Fig. 15　Top view of the landslide depositions calculated by 3DEC (the empirical formulas are shown as a red line and the summation of the red and yellow lines)**
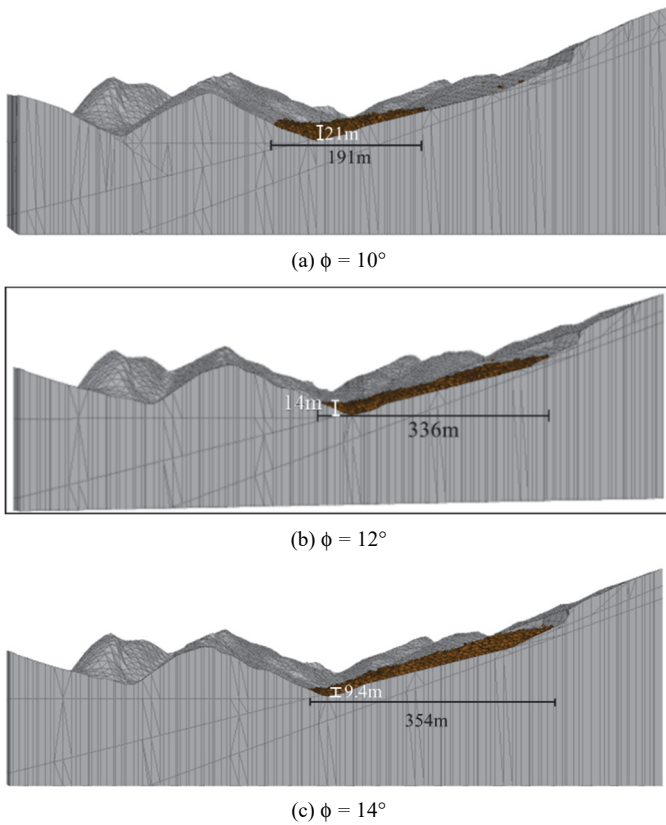
(a) $\phi = 10°$



(b) $\phi = 12°$



(c) $\phi = 14°$

**Fig. 16    Block deposition along B-B′ profile**



(a) $\phi = 10°$



(b) $\phi = 12°$



(c) $\phi = 14°$

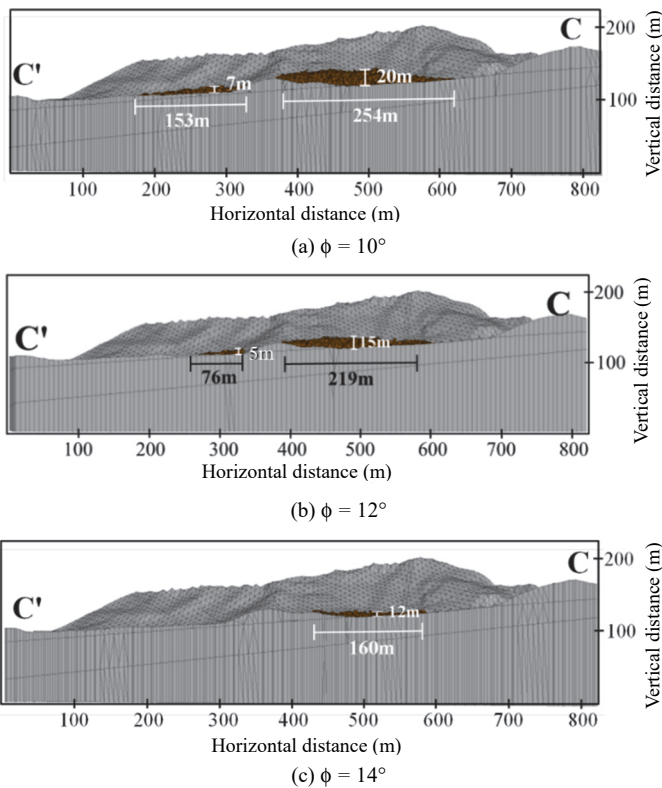**Fig. 17    Block deposition along C-C′ profile**

3DEC simulations, the height of the landslide dam along profile C-C′ is 20 m ($\phi = 10°$), 15 m ($\phi = 12°$), and 12 m ($\phi = 14°$);

thus, the variation of the height of the landslide dam is reduced compared with that obtained from the conventional statistical calculations (Kuo *et al.* 2011).

Table 3 lists the results from the empirical and statistical approach and the 3DEC simulations. Assessing the impact area using 3DEC has the following advantages over that using an empirical approach:

1. The 3DEC simulations clarify the 3D post-failure behavior of the landslide. The Nan-Shi-Keng landslide moves parallel to the dip direction of the basal sliding surface. The sliding blocks collide with the opposite hill and spread laterally upstream and downstream of the river.

2. The 3DEC simulations explicitly consider the geometry of the local landform and reduce the variations of the geometrical parameters. The computational results indicate the severe damage of the R-175 highway and classify the local houses that have high and low damage risk (Fig. 14). Table 3 provides dam geometry to evaluate the stability of the dam in the next step.

**Table 3    Movement and geometrical data from the 3DEC simulations**

| Case | | $\phi = 10°$ | $\phi = 12°$ | $\phi = 14°$ |
|---|---|---|---|---|
| Maximum velocity (m/s) / time (sec) | Crown | 14.11/30.96 | 7.85/19.33 | 6.60/10.21 |
| | Road | 19.74/24.78 | 7.40/8.66 | 5.28/9.07 |
| | Lower slope | 18.11/14.11 | 12.93/18.30 | 6.52/13.28 |
| Final displacement (m) | Crown | 277.51 | 83.52 | 47.39 |
| | Road | 290.06 | 103.73 | 53.50 |
| | Lower slope | 162.85 | 135.15 | 79.31 |
| B-B′ profile | Dam height (m) | 21 | 14 | 9.4 |
| | Horizontal distance of the depositional zone (m) | 191 | 336 | 354 |
| Landslide dam thickness along C-C′ profile (m) | This study | 20 | 15 | 12 |
| | Kuo *et al.* (2011) | 0 – 10* | | |
| Landslide dam width (m) | This study | 478 | 355 | 300 |
| | Nicoletti and Sorriso-Valvo (1991) | 232 – 552 | | |
| | Tsai *et al.* (2016) | 174 – 232 | | |
| Watershed area $A_b$ (m²) | | 588,712 | | |
| DBI | | 2.04 | 1.85 | 1.80 |

\* The landslide volume is considered as the maximum dam volume for the empirical assessment in Fig. 3 of Kuo *et al.* (2011) to be maximum dam thickness

### 5.3    Landslide Dam Stability Analysis

Ermini and Casagli (2003) proposed a dimensionless blockage index (DBI), which uses watershed area ($A_b$), dam height ($H_d$), and dam volume ($V_d$) to calculate the stability of a landslide dam:

$$\text{DBI} = \log\left(\frac{A_b \times H_d}{V_d}\right) \quad (5)$$

The watershed area upstream of the landslide dam is 588,712 m². The dam height and dam volume are individually defined as the distance and the deposit volume between the lowest point in the dam crest and the base of the valley (Nash 2003). The dam height and dam volume of the Nan-Shih-Keng landslide dam with different joint friction angles according to 3DEC simulations are presented in Table 3. The DBI of the Nan-Shih-Keng landslide ranges between 1.80 and 2.04, which is less than 2.75. Therefore,

the landslide dam is regarded as stable (Ermini and Casagli 2003).

In this study, the computation time for each case is 4 days (with an Intel Core i7-9700 CPU@ 3.00 GHz and 16 GB RAM), and the computational efficiency is the major concern when determining the block size with a joint spacing of 5 m. When the joint spacing follows the actual in situ RQD, which is 30 − 70 and 60 − 100 for the rock mass of the middle and bottom layers, respectively, the joint spacing in 3DEC simulation should be much less than 5 m. Such small joint spacing significantly increases the number of sliding blocks and thus the computation time, which may be too high to be acceptable for the current commercial 3DEC program and computer hardware. Improving the computational efficiency to simulate landslide movement with the exact in situ block size within an acceptable computation time remains a challenge. Nash (2003) provided an alternative approach to discuss the effect of the landslide dam geometry: a larger average block size generates a higher dam height. The landslide dam height from 3DEC with a joint spacing of 5 m in this study overestimates the actual potential dam height. However, the effect of block size on the impact area remains unclear. Clarifying the effect of block size on the width and length of the landslide dam is an essential topic for future study.

## 6.    CONCLUSIONS

This study successfully performed sensitivity analysis to simulate the post-failure behavior of the Nan-Shi-Keng landslide in 3D with different joint friction angles ($\phi$) and estimated the possible effect of joint friction angle on the impact area of the landslide. The computation results indicated that the R-175 highway and the farmhouses and orchards on the upper and lower slopes of the county road are at high risk to landslide impact. The sliding rocks not only move longitudinally along the sliding surface but also spread laterally after they collide with the hill on the opposite side of the river. A three-dimensional distinct element (3DEC) simulation with $\phi = 10°$ yielded the maximum landslide dam width and thickness, 478 m and 21 m, respectively. The width of the landslide dam estimated using 3DEC is consistent with that calculated using the empirical formula proposed by Nicoletti and Sorriso-Valvo (1991) but larger than that using empirical formula proposed for Taiwan by Tsai *et al.* (2016). The simulation results showed that the stable landslide dam geometry changes substantially when the joint friction angle is increased from 10° to 14°. Therefore, 3DEC is a potentially important tool for estimating the 3D impact zone of a landslide occurring on an anti-dip slope.

## ACKNOWLEDGEMENTS

## FUNDING

## DATA AVAILABILITY

The data and generated in this study are available from the corresponding author on reasonable request.

## CONFLICT OF INTEREST STATEMENT

The authors declare that there is no conflict of interest.

## REFERENCES

Busche, D. (2001). "Early Quaternary landslide of the Sahara and their significance for geomorphic and climatic history." *Journal of Arid Environments*, **49**, 429-448. https://doi.org/10.1006/jare.2001.0802

Chang, C.T. (2013). *Study on the Landslide Remediation of Tainan City Route R174*. Master Thesis, Department of Civil Engineering, National Cheng Kung University, Tainan, Taiwan (in Chinese).

Chen, Y.C. (2018). *Development of Slope Warning System for Landslides Using Radar Echo Rainfall Data*. Master Thesis, Department of Civil Engineering, National Cheng Kung University, Tainan, Taiwan (in Chinese).

Chen, K.T. and Wu, J.H. (2018). "Simulating the failure process of the Xinmo landslide using discontinuous deformation analysis." *Engineering Geology*, **239**, 269-281. https://doi.org/10.1016/j.enggeo.2018.04.002

Chien, Y.L. (2019). *Corelating the Critical Groundwater Level and Rainfall to Develop the Warning System for the Highway Slope at the Southwestern Taiwan*. Master Thesis, Department of Civil Engineering, National Cheng Kung University, Tainan, Taiwan (in Chinese). https://doi.org/10.6844/NCKU201901836

Chigira, M. (2013). *Deep-Seated Landslide*. Kinmiraisha, Nagoya, Japan (in Japanese).

Chung, M.C., Tan, C.H., Chen, M.M., and Su, T.W. (2013). "Deterministic approach for estimating the critical rainfall threshold of the rainfall-induced Nan-Shi-Keng Landslide." *Journal of Chinese Soil and Water Conservation*, **44**(1), 66-77 (in Chinese). https://doi.org/10.29417/JCSWC.201303_44(1).0006

Cundall, P.A. (1988). "Formulation of a three-dimensional distinct element model — Part I: A scheme to detect and represent contacts in a system composed of many polyhedral blocks." *International Journal of Rock Mechanics and Mining Sciences & Geomechanics Abstracts*, **25**, 107-116. https://doi.org/10.1016/0148-9062(88)92293-0

Cundall, P.A. and Strack, O.D.L. (1979). "A discrete numerical model for granular assemblies." *Geotechnique*, **29**, 47-65. https://doi.org/10.1680/geot.1979.29.1.47

Do, T.N. and Wu, J.H. (2020a). "Simulating a mining-triggered rock avalanche using DDA: A case study in Nattai North, Australia." *Engineering Geology*, **264**, 105386. https://doi.org/10.1016/j.enggeo.2019.105386

Do, T.N. and Wu, J.H. (2020b). "Simulation of the inclined jointed rock mass behaviors in a mountain tunnel excavation using DDA." *Computers and Geotechnics*, **117**, 103249. https://doi.org/10.1016/j.compgeo.2019.103249

Do, T.N. and Wu, J.H. (2020c). "Verifying discontinuous deformation analysis simulations of the jointed rock mass behavior of shallow twin mountain tunnels." *International Journal of Rock Mechanics and Mining Sciences*, **130**, 104322.

https://doi.org/10.1016/j.ijrmms.2020.104322

Ermini, L. and Casagli, N. (2003). "Predicting of the behavior of landslide dams using a geomorphological dimensionless index." *Earth Surface Processes and Landforms*, **28**, 31-47. https://doi.org/10.1002/esp.424

Fan, X., Zhan, W., Dong, X., Weste, C.V., Xu, Q., Dai, L., Yang, Q., and Huang, R. (2018). "Havenith H.B. analyzing successive landslide dam formation by different triggering mechanism: The case of the Tangjiawan landslide, Sichuan, China." *Engineering Geology*, **243**, 128-144. https://doi.org/10.1016/j.enggeo.2018.06.016

Hart, R., Cundall, P.A., and Lemos, J. (1988). "Formulation of a three-dimensional distinct element model — Part II. Mechanical calculations for motion and interaction of a system composed of many polyhedral blocks." *International Journal of Rock Mechanics and Mining Sciences & Geomechanics Abstracts*, **25**, 117-125. https://doi.org/10.1016/0148-9062(88)92294-2

Itasca. (2016a). *3 Dimensional Distinct Element Code Theory and Background*. Itasca Consulting Group, Inc., Minnesota, USA.

Itasca. (2016b). *3DEC Version 5.2 Command Reference*. Itasca Consulting Group, Inc., Minnesota, USA

Kao, C.C. (2006). *The Study on Definition of Slope Sliding Surface — A Case of Wu-Shan Landslide Area*. Master Thesis, Department of Civil and Disaster Prevention, National Taipei University of Technology, Taipei, Taiwan (in Chinese).

Kao, Y.T. (2014). *Study of Failure Plane — A Case of County Road Number 174*. Master Thesis. Department of Civil Engineering, National Taipei University of Technology, Taipei, Taiwan (in Chinese). https://doi.org/10.6841/NTUT.2006.00172

Kuo, Y.S., Tsang, Y.C., Chen, K.T., and Shieh, C.L. (2011). "Analysis of landslide dam geometries." *Journal of Mountain Science*, **8**, 544-550. https://doi.org/10.1007/s11629-011-2128-1

Land Engineering Consultants Co. (2006). *Report of the First Phase of Surveying, Design, Borehole Drilling, and Monitoring on the Roadbed Protecting Measures at 50k+650 on Country Road Number 174*. Fifth Maintenance Office, Ministry of Transportation and Communication, Chiai, Taiwan (in Chinese).

Land Engineering Consultants Co. (2019). *Report of the Landslide Investigations and Slope Monitoring on the Tainan City Highway 174 at the Mileage of 50k+500*. Tainan City Government, Taiwan (in Chinese).

Lo, C.M. (2017). "Evolution of deep-seated landslide at Putanpunas stream." *Geomatics, Natural Hazards and Risk*, **8**, 1204-1224. https://doi.org/10.1080/19475705.2017.1309462

Nash, T.R. (2003). *Engineering Geological Assessment of Selected Landslide Dams Formed from 1929 Murchison and 1968 Inangahua Earthquakes*. Ph.D. Dissertation, University of Canterbury, Christchurch, New Zealand. http://dx.doi.org/10.26021/6643

Nicoletti, P.G. and Sorriso-Valvo, M. (1991). "Geomorphic controls of the shape and mobility of rock avalanches." *Geomorphic Controls of Rock Avalanches*, **103**, 1365-1373. https://doi.org/10.1130/0016-7606(1991)103<1365:gcotsa>2.3.co;2

Palmstrom, A. (2005). "Measurements of and correlations between block size and rock quality designation (RQD)." *Tunnelling and Underground Space Technology*, **8**, 362-377. https://doi.org/10.1016/j.tust.2005.01.005

Scheidegger, A. (1973). "On the prediction of the reach and velocity of catastrophic landslides." *Rock Mechanics*, **5**, 231-236. https://doi.org/10.1007/BF01301796

Su, K.H. (2007). *Investigating the Slope Failure of Interbedded Sandstone and Mudstone Slope: Case of Highway 174 on 50k+650*. Master Thesis, Department of Resources and Environment, Leader University, Tainan, Taiwan (in Chinese).

Tsai, Y.J., Lai, W.C., Hsu, T.C., Hsieh, C.L., and Huang, H.Y. (2016). "Assessment of the impact area for large-scale landslides." *Journal of the Taiwan Disaster Prevention Society*, **8**(2), 159-172 (in Chinese).

Van Woerden, T.H. (2018). *Quaternary Geology and Landslide Dam Hazard Assessment of the Shotover Gorge, Otago*. Master Thesis, Department of Disaster Risk and Resilience, University of Canterbury, Queenstown, New Zealand. http://dx.doi.org/10.26021/6160

Wu, J.H. (2010). "Compatible algorithm for integrations on a block domain of any shape for three-dimensional discontinuous deformation analysis." *Computers and Geotechnics*, **37**(1-2), 153-163. https://doi.org/10.1016/j.compgeo.2009.08.009

Wu, J.H., Do, T.N., Chen, C.H., and Wang, G. (2017a). "New geometric regulation for the displacement constraint points in discontinuous deformation analysis." *International Journal of Geomechanics*, **17**(5), E4016002-1~E4016002-18. https://doi.org/10.1061/(ASCE)GM.1943-5622.0000648

Wu, J.H. and Hsieh, P.H. (2021). "Simulating the postfailure behavior of the seismically-triggered Chiu-fen-erh-shan landslide using 3DEC." *Engineering Geology*, **287**, 106113. https://doi.org/10.1016/j.enggeo.2021.106113

Wu, J.H., Lin, W.K., and Hu, H.T. (2017b). "Assessing the Impacts of a Large Slope Failure using 3DEC: The Chiu-fen-erh-shan Residual Slope." *Computers and Geotechnics*, **88**, 32-45. https://doi.org/10.1016/j.compgeo.2017.03.002

Wu, J.H., Lin, W.K., and Hu, H.T. (2018). "Post-failure simulations of a large slope failure using 3DEC: The Hsien-du-shan slope." *Engineering Geology*, **242**, 92-107. https://doi.org/10.1016/j.enggeo.2018.05.018

Yang, G., Qi, S., Wu, F., and Zhan, Z. (2018). "Seismic amplification of the anti-dip rock slope and deformation characteristics: A large-scale shaking table test." *Soil Dynamics and Earthquake Engineering*, **115**, 907-916. https://doi.org/10.1016/j.soildyn.2017.09.010